ingegneria sismica
International Journal of Earthquake Engineering
Anno XLIII - Num. 1 - 2026

Construction of an optimization method for regulating initial residual stress during machining of high-strength aluminum alloys

Haichao Ye[1,*], *Yiping Xu*[1], *Fangfei Chang*[1], *Shaoshuai Hou*[1] *and Sicheng He*[1]

[1] School of Intelligent Manufacturing, Luoyang Institute of Science and Technology, Luoyang, Henan, 471023, China

SUMMARY: *This study investigates the effect of different shrinkage rates and residual stresses between the elements of high-strength aluminum alloy during machining, which will affect the performance of high-strength aluminum alloy and cause significant economic losses to the manufacturer. In order to solve this problem, a finite element model of high-strength aluminum alloy laminar cooling heat–force coupling is established in the ABAQUS platform to simulate the thermal field, phase change, and residual stress development during the cooling process. The residual stresses of the high-strength aluminum alloy blank are obtained by the drilling method. The results show that the error between simulation and experimental measurement is between 6.52% and 13.68%, proving that the finite element model established in this study is accurate. It is concluded from further research that the convective heat transfer coefficient is the main influence on the residual stress of quenched aluminum alloy. Thus, this paper suggests that it is feasible to regulate residual stress through the convective heat transfer coefficient, thereby achieving quality control of high-strength aluminum alloy components at the source.*

KEYWORDS: *High-strength aluminum alloy; Residual stress control optimization; Finite element simulation; Quenching process; Mechanical processing*

1 Introduction

The entire aerospace, automotive and other manufacturing industries can not do without a large number of high-quality aluminum. Compared with the general aluminum alloy, high-strength aluminum alloy has more superior performance, such as lower density, improved strength, in order to ensure the lightweight at the same time to ensure the stiffness required by the parts, hot machining is easier to deal with, fatigue life has been greatly improved, etc., these performance enhancements have made high-strength aluminum alloys to become the main structural materials in the manufacturing industry in aerospace and so on [1-5].

Aluminum alloy materials are very widely used in aerospace and other applications, mainly used to manufacture high-strength, high stress corrosion resistance, high fracture toughness of structural components, such as aircraft landing gear, fuselage frames, wing beams, spacer frames, wing ribs, etc. [6, 7]. In the manufacture of large aircraft, aluminum alloy is a considerable proportion. For example, the proportion of aluminum alloy in the materials used in Boeing777 is 70%, the proportion of aluminum alloy in Airbus A380 is 61%, and the proportion of aluminum alloy in the C919 airframe in China is 70% [8, 9]. Residual stress is a kind of internal force inside the material, which can always keep the balance of its own stress under the action of no external force. In the preparation or processing of aluminum alloy

*yehc@lit.edu.cn
https://doi.org/10.65102/is2026176
Published: 30 April, 2026

materials, the residual stresses generated within the material will not only affect the mechanical properties of the aluminum alloy sheet, but also affect the processing quality of the material, and in serious cases, the risk of cracking will occur, resulting in product obsolescence [10, 11]. When performing high-speed machining of high-strength aluminum alloy structural parts, the effect of the initial residual stress field of the workpiece becomes more and more pronounced. Thus, it is necessary to research the generation mechanism of the initial residual stress field of high-strength aluminum alloy during the machining process and assess the effects thereof on machining distortion.

Deformation caused by machining operations continues to be a worldwide problem in manufacturing precise aluminum alloy products, whereby the distribution and development of residual stress depend on various variables, including the thickness of the material being machined. For instance, Xue et al. have formulated a mathematical model and finite element analysis to explore the correlation between residual stress and deformation while machining 2219 aluminum alloy rolled rings. From their study, initial residual stresses ranging from 40 to 80 MPa lead to an elliptical deformation of the workpiece, where the highest deformation value attained is 0.4 mm [12]. Yi et al. performed milling tests using 7075 aluminum alloy samples and found out that residual stress influences depths below 0.12 mm, whereby end milling causes higher stress depths compared to flank milling. Using their findings, they formulated a regression and neural network-based predictive model that aids in deformation control while machining [13]. Zhang et al. conducted experiments and discovered that a relatively thin 3 mm aluminum alloy plate has a shallow and low-level compressive stress layer, whereas a thick 9 mm plate shows a deep and significant compressive stress layer. The importance of thickness and stiffness in stress distribution cannot be underestimated [14]. Finally, Teng et al. proposed a finite element model for gravity extrusion joint machining in thick 2219 aluminum alloy plates at high speed and observed that longitudinal residual stresses were larger than transverse stresses, and those in the forward direction were more significant than those in the backward direction [15].

Many experts, scholars and engineers have carried out a lot of theoretical research work on the problem of regulating aluminum alloy machining residual stresses from the machining sequence, tool path, cutting parameters, clamping layout and other process solutions. Wu et al. presented a finite element analysis model considering the rolling and heat treatment processes to alleviate machining-induced deformation of aerospace rolled rings made from 2219 aluminum alloy. Their findings showed that stress-relieving heat treatment greatly alleviates initial residual stress, resulting in homogeneous distribution, which controls deformation during machining of massive thin-walled rings [16]. Ma et al. proposed an expansion homogenization method to solve the problem of initial residual stress in super-large rolled rings made from 2219 aluminum alloy. Finite element simulation confirmed that residual stress was alleviated by more than 40%, with maximum stress reduced to 65 MPa, thus effectively controlling the processing deformation of thin-walled rings [17]. Zheng et al. established an ultrasonic rolling stress prediction model considering initial residual stress and plastic compressive depth for 7075 aluminum alloy. The model suggested that static load, amplitude, and relevant parameters could control residual compressive stress layer, and the model error was less than 10%. Thus, the prediction model had high credibility [18]. Xu et al. compared residual stress distribution in aluminum alloy Al-7075-T6 subjected to one and several cutting operations. The results indicated that multiple cutting procedures could significantly decrease the surface tensile stress and subsurface compressive stress intensity and thickness, laying a foundation for cutting optimization to avoid deformations in workpieces [19]. Li et al. proposed a new technique to relieve residual stresses in aluminum alloy parts using pulsed strong magnetic fields. Non-contact Lorentz force technology causes plastic deformation and effectively reduces residual

stresses within milliseconds, as proven experimentally with stress relief ratio up to 84.9% in large aluminum rings [20]. Xu et al. optimized the morphology and applied thermal vibration stress-relief treatment to increase equivalent bending stiffness and decrease maximum deformation and residual stress of thin-walled 7075 aluminum alloy part [21].

Moreover, Ye et al. suggested the intermittent quenching method aimed at lowering the yield strength of the material through avoiding the effect of precipitation hardening during quenching. The effectiveness of such technique was proven experimentally as the authors demonstrated how this process helped to minimize residual stresses in thick plates made of 7050 aluminum alloy after quenching [22]. Zhang et al. used both computational simulation techniques and experimental research for studying the development of residual stresses in 7050 aluminum alloy during heat treatment [23]. They showed that uphill quenching combined with aging can reduce quenching stresses by 55%, minimizing and homogenizing initial stresses. Chen et al. demonstrated an exponential decrease in residual stresses with increasing annealing temperature, along with grain refinement, but high-temperature annealing also resulted in a significant decrease in material strength and hardness [24]. Li et al. experimentally showed that stress-relaxation annealing method treated at 160°C for 8 h resulted in a 55.83% reduction of residual stresses while maintaining the tensile strength and elongation of the material, revealing a synergistic relaxation mechanism of creep and deformation [25]. Pan et al. developed a laser impact strengthening technique based on low pulse energy for modulation of residual stresses in thin-walled AA7075 aluminum alloys, which can also be used to significantly enhance the high circumferential fatigue limit of the specimens under deformation-free conditions through dynamic nanoprecipitation and dislocation proliferation [26]. Through simulations and experiments, Qi et al. confirmed that elevated laser power exacerbates the melt pool temperature gradient, increasing the residual stress from 85.9 MPa to 169.7 MPa, and that optimization of the process parameters can regulate the stress, providing a way to reduce the initial residual stress [27]. However, the research on aluminum alloy fabrication and cutting and forming of monolithic structural components has been cut-throat so far, and is currently centered around two single technologies, namely, quench-based control methods, numerical simulation and validation methods for machining deformation. The control and abatement techniques for residual stresses lack corresponding attention, and there is a lack of composite residual stress analysis for multiple machining processes under complex processes.

In this study, an effective technical path for initial residual stress regulation and optimization is constructed by using the finite element simulation method. By introducing the thermal-elastic-plastic theory and considering the phase transition effect, a finite element model is established, through which the thermal-force coupling behavior during the machining process of high-strength aluminum alloys is reflected and the evolution law of residual stresses is revealed. In order to verify the reliability of the method, 7075 aluminum alloy and 7449 aluminum alloy, which are widely used, are taken as the research objects. In terms of residual stress verification, the drilling method and MTS3000 residual stress analyzer are used to accurately measure the actual stress value, which provides calibration data reference for the simulation model. In terms of process validation and optimization, several groups of controlled experiments were designed to verify the practical application of the proposed initial residual stress regulation and optimization method.

2 High-strength aluminum alloy machining initial residual stress regulation optimization method

The application of aluminum alloys in aerospace engineering and other industries where

integral thin-walled structures are used is very common. To obtain the proper mechanical properties such as strength and toughness, solution heat treatment is necessary. The quenching of aluminum alloys involves an elaborate thermomechanical process. Even though quenching improves the strength and hardness of the material, it creates quenching residual stress. Quenching residual stress in aluminum alloy billets plays an important role in causing deformation when thin-walled parts are fabricated. Therefore, it is essential to investigate the impact of quenching residual stress on the deformation caused by the milling of thin-walled parts. In this chapter, numerical simulations of the quenching process of aluminum alloys will be performed to identify the thermal stress caused by quenching. This will give us the initial residual stress state that can be utilized for further finite element analysis in the next chapter.

2.1 Theoretical foundations of numerical simulation

2.1.1 Mathematical model of quenching process

For a three-dimensional part, the quench thermal conductivity equation is:

$$\frac{\partial}{\partial x}\left(\lambda\frac{\partial T}{\partial x}\right)+\frac{\partial}{\partial y}\left(\lambda\frac{\partial T}{\partial y}\right)+\frac{\partial}{\partial z}\left(\lambda\frac{\partial T}{\partial z}\right)=\rho C\frac{\partial T}{\partial t} \tag{1}$$

Among them, λ represents the thermal conductivity coefficient $\left(\mathrm{W/m\cdot K}\right)$, ρ represents the density $\left(\mathrm{Kg/m^3}\right)$, and C represents the specific heat capacity $\left(\mathrm{J/Kg\cdot K}\right)$; T denotes temperature $\left(\mathrm{K}\right)$; t denotes time $\left(\mathrm{s}\right)$. For the quenching process, the specific heat capacity and heat transfer coefficient are related to the temperature at which the material is quenched.

When the part is quenched, the boundary condition is considered to be a convective heat transfer boundary condition, i.e., the:

$$-\lambda\frac{\partial T}{\partial n}\Big|_{\tau}=h\left(T_s-T_q\right) \tag{2}$$

where λ denotes the heat transfer coefficient; $\frac{\partial T}{\partial n}$ denotes the temperature gradient along the direction; - denotes the direction of heat flow to the temperature decrease; h denotes the surface heat transfer coefficient; τ denotes the boundary of the heat transfer; T_s denotes the temperature of the surface of the part; T_q denotes the temperature of the quenching medium.

Aluminum alloy quenching process is a complex thermal coupling process, quenching heat treatment stress generation does not involve the external load, including only the temperature gradient, tissue transformation caused by thermal stress, as well as different temperature conditions, the aluminum alloy material mechanical properties of the change caused by the additional stress, etc., which belongs to the thermal - elastic-plasticity problem, the theoretical basis for the calculation of the thermal stress field is the theory of thermoelasticity.

2.1.2 Theory of Thermoelasticity and Plasticity in Quenching Processes

Based on the aforementioned formula of heat conduction and boundary conditions, the distribution pattern of temperature field can be obtained when quenching the aluminum alloy blank, and the result of temperature field analysis provides boundary conditions for the next

thermal stress analysis. When the workpiece is quenched, there will be significant temperature variations within the material, leading to the formation of elastic and plastic strains. The assumptions adopted for mechanical analysis are as follows:

(1) Material isotropy;

(2) The yielding process of the material obeys the Mises yield criterion;

(3) the plastic region obey the isotropic strengthening of the flow law, that is, Prandtl-Reuss plastic flow increment theory.

The full strain increment in the quenching process is expressed as:

$$d\left\{\varepsilon\right\} = d\left\{\varepsilon_e\right\} + d\left\{\varepsilon_p\right\} \tag{3}$$

where $d\{\varepsilon_e\}$ denotes elastic strain and $d\{\varepsilon_p\}$ denotes plastic deformation. The $d\{\varepsilon_e\}$ and stress increment $d\{\sigma\}$ are in accordance with the generalized Hooke's law, and the $d\{\varepsilon_p\}$ and stress increment $d\{\sigma\}$ are in accordance with the flow law.

When a material is elastic or plastic, the relationship between stress and strain is:

$$\{d\sigma\} = [D]\{d\varepsilon\} - \{C\}dT \tag{4}$$

where $\left[D\right]$ is the elastic or plastic matrix and $\{C\}$ is the temperature-dependent vector.

in the elastic region:

$$[K] = [D]_e \tag{5}$$

$$\{C\} = \{C\}_e = [D]\left(\{\alpha\} + \frac{\partial[D]_e^{-1}}{\partial T}\{\sigma\}\right) \tag{6}$$

where $\{\alpha\}$ denotes the linear expansion coefficient vector and T denotes the temperature.

In the plastic region, the yield stress is also temperature dependent and the yield criterion is expressed as:

$$\bar{\sigma} - H\left(\int d\bar{\varepsilon}_p, T\right) = 0 \tag{7}$$

Its differential form is expressed as:

$$\left\{\frac{\partial\bar{\sigma}}{\partial\{\sigma\}}\right\}^T d\sigma = H' d\bar{\varepsilon}_p + \frac{\partial H'}{\partial T}dT \tag{8}$$

Law of Mobility for:

$$d\{\varepsilon_p\} = d\bar{\varepsilon}_p \frac{\partial\bar{\sigma}}{\partial\{\sigma\}} \tag{9}$$

$$d\bar{\varepsilon}_p = \frac{\left\{\frac{\partial\bar{\sigma}}{\partial\{\sigma\}}\right\}[D_e](d\{\varepsilon\} - d\{\varepsilon_\tau\} - d\{\varepsilon_0\}) - \frac{\partial H'}{\partial T}dT}{H' + \left\{\frac{\partial\bar{\sigma}}{\partial\{\sigma\}}\right\}^T [D_e]\frac{\partial\bar{\sigma}}{\partial\{\sigma\}}} \tag{10}$$

The elasticity matrix is expressed as:

$$[D]_{ep} = [D]_e - [D]_p \tag{11}$$

$$[D]_p = \frac{[D_e]\frac{\partial\bar{\sigma}}{\partial\{\sigma\}}\left\{\frac{\partial\bar{\sigma}}{\partial\{\sigma\}}\right\}^T [D_e]}{H' + \left\{\frac{\partial\bar{\sigma}}{\partial\{\sigma\}}\right\}^T [D_e]\frac{\partial\bar{\sigma}}{\partial\{\sigma\}}} \tag{12}$$

$$[C]_{ep} = [D]_{ep}\{\alpha\} + [D]_{ep}\frac{\partial[D]_e^{-1}}{\partial T}\{\sigma\} - \frac{[D]_e\frac{\partial\bar{\sigma}}{\partial\{\sigma\}}\frac{\partial H}{\partial T}}{H' + \left\{\frac{\partial\bar{\sigma}}{\partial\{\sigma\}}\right\}^T [D_e]\frac{\partial\bar{\sigma}}{\partial\{\sigma\}}} \tag{13}$$

Here $\frac{\partial\bar{\sigma}}{\partial\{\sigma\}}$ is the partial derivative of the scalar function $\bar{\sigma}$ with respect to the vector $\{\sigma\}$, and H' is the partial derivative of the functional plastic strain $H\left(\int d\bar{\varepsilon}_p, T\right)$ as the partial derivative of the function plastic strain.

For a cell in the structure, its equilibrium equation is:

$$\{dF\}^e + \{dR\}^e = [K]^e\{d\delta\}^e \tag{14}$$

where $\{dF\}^e$ denotes the unit nodal force increment, $\{dR\}^e$ denotes the temperature-induced unit stress increment, $\{d\delta\}^e$ denotes the nodal displacement increment, and $[K]^e$ denotes the unit stiffness matrix.

$$[K]^e = \int [B]^T[D][B]dV \tag{15}$$

$$\{dR\}^e = \int [B]T\{C\}dTdV \tag{16}$$

where $[B]$ denotes the relationship matrix between cell strain and node displacement. Replacing $[D]$, $[C]$ with $[D]_e$, $\{C\}_e$ or $[D]_{ep}$, $[C]_{ep}$ to form the unit stiffness matrix and the equivalent nodal loads, and then forming the total stiffness matrix $[K]$ and the total loads $\{dF\}$, the equilibrium equations obtained are:

$$[K]\{d\delta\} = \{dF\} \tag{17}$$

The thermoelastic stress-strain solution process is to add the temperature increment to a finite number of units of the workpiece, each temperature increment corresponds to the displacement increment of each node, the unit strain increment and the unit node displacement increment relationship equation can be expressed as:

$$\{d\varepsilon\}^e = [B]\{d\delta\}^e \tag{18}$$

After finding the strain, then according to the stress-strain relationship equation, the unit stress increment can be found, and also find the quenching process of stress and strain process and the final residual stress.

2.2 Finite element model for the evolution of residual stresses in aluminum alloy machining process

2.2.1 Simulation process of laminar flow cooling of high strength aluminum alloy

Considering the open area of the collector during the cooling process for hot rolling of high strength aluminum alloys in a manufacturing plant, the following five stages can be distinguished in the laminar flow cooling of high strength aluminum alloys: air cooling, ultra-fast cooling, air cooling, laminar cooling, and air cooling. This cooling method is used in the FEA modeling.

2.2.2 Finite element model geometry

The geometry of the finite element model for the studied high-strength aluminum alloy in this chapter is based on the exact dimensions of the used steel plate on the production line. This plate is considered as an infinitely long plate in the longitudinal direction, and hence, in order to make the numerical simulation accurate, the length of the model is chosen to be 3200 mm, resulting in total dimensions of 3200 mm × 1500 mm × 4.2 mm. Here, X, Y and Z represent the length, width, and thickness directions of the model, respectively. Since the geometrical features of the plate determine that the length should be segmented by 50 parts, the width direction involves a finer mesh of 15 cells close to each edge while 35 cells in the central zone of the plate. On the other hand, the thickness is segmented into 4 parts, which produces cell thickness of 1.05 mm. The used hexahedral C3D8R elements have reduced integration and hourglass control to calculate stress. Due to the complex stress field near the edges in the plate because of edge cooling, the mesh of edges was refined to increase calculation accuracy.

2.2.3 Thermophysical parameters

The modeling of the laminar cooling of the high-strength aluminum alloy using finite elements is a nonlinear computation process. It means that accurate values of the thermophysical properties for this material should be obtained. The current chapter contains the experimentally derived values of strength, specific heat, and thermal expansion coefficients of the high-strength aluminum alloy depending on temperature. Moreover, the temperature dependency of elastic modulus, thermal conductivity, Poisson’s ratio, and density are computed using software JMatPro.

2.2.4 Initial temperature setting

Based on infrared temperature measurement results, the temperature of the high-strength aluminum alloy after passing through the finishing rolling rack reaches 475° C. This data becomes the basis for establishing the initial temperature of uniform thickness distribution in

the finite element model. For the crimping procedure, the cooling final temperature is specified as 110° C. In reality, along with the heat transfer effect caused by contact with the rolls, heat transfer across the plate width takes place due to air radiation of its edges, which leads to lower edge temperatures than those at the center. Thus, in reality, upon entering the cooling system track, the high-strength aluminum alloy features a certain temperature discrepancy between the edge and center. To examine the impact of the transverse temperature discrepancy on the residual stress, a finite element model accounting for different transverse initial temperature distributions will be created in this chapter.

2.2.5 Boundary condition setting

The convective heat transfer during the cooling of high strength aluminum alloy mainly involves heat transfer from air to steel, heat transfer from water to steel, and heat radiation. The formula for calculating the convective heat transfer coefficient from air to steel is stated below:

$$h_{ac} = \frac{\varepsilon\sigma_0(T_\infty^4 - T^4)}{T_\infty - T} = \varepsilon\sigma_0(T_\infty^2 + T^2)(T_\infty + T) \tag{19}$$

where: h_{ac} is the convective heat transfer coefficient of air cooling $\left(\mathrm{m}^2 \cdot \mathrm{K}\right)$; ε is the emissivity of the steel, generally taken as 0.8~1.0; σ_0 is Stefan Boltzman's constant, taken as $.5.67\times10^{-8}\mathrm{W/(m\cdot K^4)}$; T_∞ is the surface temperature of the high-strength aluminum alloy $\left(^\circ\mathrm{C}\right)$; T is the ambient temperature $\left(^\circ\mathrm{C}\right)$.

In the case of high-strength aluminum alloys, the water cooling method is mainly determined by the properties of the cooling water, the surface temperature, the steel plate, and the convective heat transfer coefficient between the cooling water and the steel plate. Therefore, the average heat transfer coefficient is given as follows:

$$H^w = \frac{9.72\times10^5\omega^{0.355}}{T - T_w} \times \left[\frac{(2.5 - 1.5\lg T_w)D}{P_l P_c}\right]^{0.645} \times 1.163 \tag{20}$$

where: H^w is the average heat transfer coefficient $\left(\mathrm{W/m^2\cdot K}\right)$; ω is the current density $\left(\mathrm{m^3/(min\cdot m^2)}\right)$; T is the surface temperature of the steel plate $\left(^\circ\mathrm{C}\right)$; T_w is the cooling water temperature $\left(^\circ\mathrm{C}\right)$; P_l is the nozzle spacing $\left(\mathrm{m}\right)$ along the rolling line direction; P_c is the adjacent nozzle spacing $\left(\mathrm{m}\right)$ in the vertical rolling line direction; D is the nozzle diameter $\left(\mathrm{m}\right)$.

2.2.6 Phase transition modeling

During the laminar cooling of high-strength aluminum alloy, there is a quick reduction in temperature that triggers phase changes, altering the structure from the final austenitic rolled condition to ferrite, pearlite, martensite, and other organizational structures. The phase change from austenite to the rest of the structures can be classified into diffusion control phase change and non-diffusion control phase change. In diffusion controlled phase change, the major changes observed are those from ferrite, pearlite, and bainite; all these require atomic diffusion that takes place over a long time period, and incubation period for the process of change plays a significant role in the process.

(i) Diffusive phase transformation

The diffusive phase transformation model contains the kinetic equation of phase transformation and the thermodynamic equation of phase transformation. The kinetic equation determines what kind of phase transformation occurs in steel and the amount of transformation, while the thermodynamic equation of phase transformation controls when the phase transformation occurs, and both of them are indispensable. Since the phase transformation of high-strength aluminum alloys in the laminar cooling stage is a non-isothermal transformation process with continuous cooling, the JMAK equation can be used to describe the phase transformation in the austenitic cooling process. At the same time, the principle of additivity of the phase transition gestation period can be used for the operation, and its calculation formula is as follows:

$$X = 1 - \exp(-Kt^n) \tag{21}$$

$$t_h = \left[\frac{\ln(1 - X_i)}{K} \right]^{\frac{1}{n}} \tag{22}$$

$$t_{i+1} = t_h + \Delta_t \tag{23}$$

where: X is the phase change volume fraction; K, n are parameters related to the phase transition, determined from isothermal transition data; t_h is the time (s) required to transform X_i at the temperature at the beginning of the time step; t_{i+1} is the phase transition virtual time (s) at the $i+1$ th time step; Δt is the step size (s) of the $i+1$ th time step.

The non-isothermal transformation equation for continuous cooling of high-strength aluminum alloy can be obtained by collation:

$$X_{i+1} = 1 - \exp\left[-K_{i+1}(t_{i+1} + \Delta t)\right]^n \tag{24}$$

The phase change thermodynamic model describes the accumulation of the gestation period in a continuous cooling process discretized into an isothermal accumulation process at multiple temperatures. Assuming that the temperature at the beginning is T_i corresponding to the step size of the i th time step is Δt_i, and the phase change gestation period at the T_i th temperature is τ_i, the accumulation of the i th time step over the entire phase change gestation period is:

$$\frac{\tau_i}{\tau_i(T_i)} \tag{25}$$

Then the phase transition gestation period of the continuous cooling process is:

$$\int_0^n \frac{\tau_i}{\tau_i(T_i)} \tag{26}$$

(ii) non-diffusive phase transformation

Martensite transformation belongs to the non-diffusive phase transformation, the relationship between its transformation and temperature is:

$$X = 1 - \exp\left[-\alpha(M_s - T)\right] \tag{27}$$

where X is the volume fraction of martensite transformation, %; α is the martensite transformation rate constant; and Ms is the martensite onset of transformation temperature.

(iii) latent heat of phase transition

Supercooled austenite to ferrite and other organizational transformation is a high-energy to low-energy transformation process, the process will release heat, known as the latent heat of phase transition, so the calculation process needs to take into account the influence of the latent heat of phase transition, which is calculated by the formula:

$$q = \Delta H_i \frac{\Delta X_i}{\Delta t_i} \rho \tag{28}$$

where: q is the heat (J) of supercooled austenite during complete phase transformation at the time-synchronized starting temperature; ΔH_i is the enthalpy of enthalpy release from complete phase transformation of austenite at the I th incremental step $\left(\mathrm{MJ/m^3}\right)$; ΔX_i is the increment of the volume fraction of the phase transition in the i th time step; Δt_i is the step length of the i th incremental step (s); ρ is the material density $\left(\mathrm{kg/m^3}\right)$.

The programming process will use the Fortran programming language that comes with the Visual Studio application in order to construct the phase transition dynamics model. Additionally, the two ABAQUS user subroutine, USDFLD and HETVAL will be used in order to allow coupling between the three fields.

3 Optimized Finite Element Simulation of Aluminum Alloy Initial Residual Stress Regulation

3.1 Example of Finite Element Simulation Verification of Quenching Residual Stresses

Since 7449 and 7075 aluminum alloys are both Al-Zn-Mg-Cu series materials, their chemical compositions are relatively similar. The stress distribution in quenched 7075 alloy is numerically simulated and then validated against experimental measurements. To constrain the displacement degrees of freedom in the XYZ, XZ, and Z directions during thermo-mechanical analysis, three points on the lower surface of the specimen are selected, as illustrated in Figure 1. The numerical predictions are then checked against the measured data. It can be seen that, although differences exist in the magnitudes at several positions, this is because, despite their similar compositions, slight variations in elemental proportions lead to differences in mechanical and thermophysical properties; however, the overall trend of the curves remains essentially consistent. In the X-direction, for example, the measured stress reaches 350 MPa at a distance of 0, whereas the computed value is 352 MPa. The calculated result of 352 MPa also indicates that the stress profiles after quenching in the two alloys are generally similar, characterized by surface compression and internal tension. Along the Z-direction, the stress values for both materials vary only slightly from 0 to 105 mm, increase over the range of 105 to 120 mm, and then decline more rapidly, with minimum values of -185 MPa for 7449 alloy and -240 MPa for 7075 alloy. Based on the above qualitative and quantitative evaluation, it can be concluded that the finite-element predictions of stress after quenching are credible.

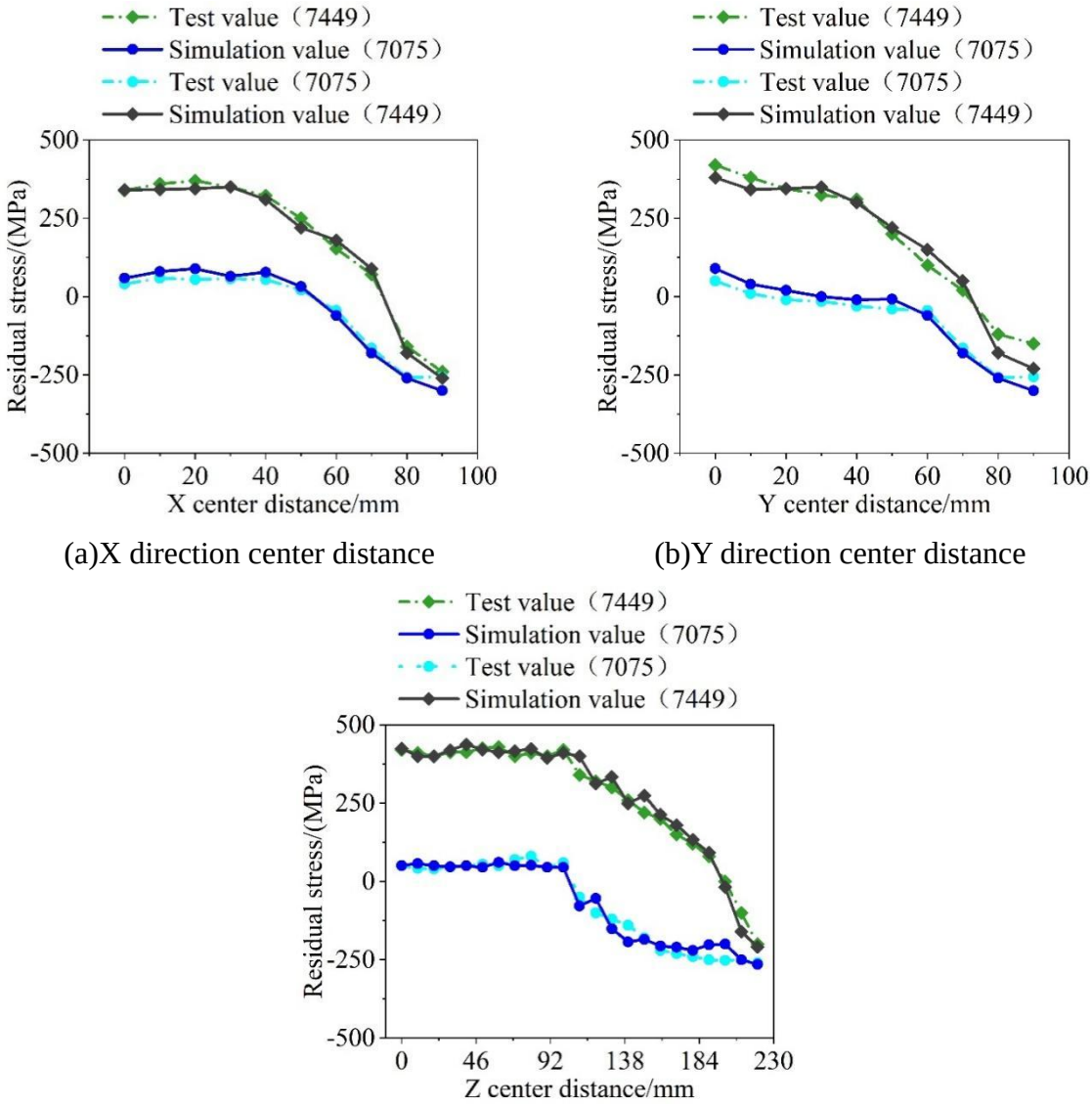

(a)X direction center distance (b)Y direction center distance

(c)Z direction center distance

Figure 1: Simulation results are compared with the actual test data

3.2 Finite element simulation of rough machining process

Material selected for blank was 7075 Aluminum Alloy. The thermophysical and mechanical properties data for 7075 alloy is summarized in Table 1. The meshing used in finite element modeling and residual stress distribution have been identified for heat transfer and thermal stress analysis for which meshing type is used DC3D8 while for residual stress analysis type of mesh is C3D8R. Here the radial residual stress is mainly compressive with tensile stress limited to small area.

Table 1: Thermal physics and mechanical properties of aluminum alloy

Temperature/°C	20	100	150	200	250	300	400
Elastic modulus/GPa	71.5	65.2	60.2	56.5	37.9	31.4	24
Yield stress /MPa	455.6	389.4	346.2	275.6	47.2	35.6	15.2
Heat conductivity (W/(m·°C)	114.2	128.5	135.2	142.1	153.2	160.9	165.3
Specific heat (J/(kg·°C)	834.2	897.6	916.2	975.2	1012.6	1125.5	1209
Thermal expansion coefficient (10^{-6}·°C^{-1})	21.5	23.2	/	24.2	25.3	30.5	31.6
Convection heat transfer coefficient (W/(m^2·°C)	2600	5100	11000	13856	1200	3200	680

3.3 Residual Stress Measurement and Analysis

Aluminum alloy billet thickness is large, without affecting the machining, the less destructive drilling method is utilized, and the measurement is carried out by using MTS3000 type residual stress analyzer. Table 2 compares the simulation result of the residual stress with the experimental value measured at the mid-line of the billet outer surface at four different points, which are equally distant from each other, as measured at the same angle. The difference between the simulation and experiment value is from 6.52% to 13.68%, wherein the experimental value is smaller than that of the simulation. This is due to the assumption of an ideal situation in the finite element model simulations. The temperature of the water cannot be kept constant, and human errors associated with the operation of the equipment are not negligible. The simulation assumes that there is no internal residual stress in the aluminum alloy before the quenching process. On the other hand, there is always internal residual stress before quenching.

Table 2: The residual stress simulation is compared with the measurement results

Measuring point	Simulation result/(MPa)	Measurement result/(MPa)	Error/%
1	77.245	72.212	6.52
2	94.212	85.261	9.50
3	77.254	69.658	9.83
4	95.624	82.541	13.68

3.4 Cutting Process and Deformation Measurement Analysis of Thin-Walled Rotating Structural Parts

After the end of workpiece cutting, measure the radial deformation of the workpiece in two sets of paths. Path 1 is to measure 8 points equidistant from the outer circle, and select the starting point as the measurement zero point; path 2 is to measure 7 points in the axial direction sequentially, and select the middle position as the measurement zero point. The measurement results are compared with the finite element simulation results for verification.

According to the above method to measure the radial deformation of the two paths of the processed thin-walled rotary structural components, the obtained path 1 radial deformation and path 2 radial deformation data are shown in Table 3 and Table 4, respectively.

Path 1 features a radial deformation pattern in which there will be first an increase, then a reduction, and then an increase again. In terms of magnitude, the highest value is 0.153 mm in the experiment whereas the highest value is 0.162 mm through the simulation process. Path 2 involves a reduction first and then an increase to result in the creation of two convexities and one concavity on the workpiece. The highest radial deformation value in the experiment is 0.150

mm whereas the highest radial deformation through the simulation process is 0.172 mm.

There do exist certain differences between the simulation and the experiments done. The deformation caused according to the simulation is greater than the deformation found in the experiment. A comparison of the residual-stress simulation and the experiment shows that the residual stress of the blank estimated using the simulation model is greater than the actual one. The simulation is performed based on ideal conditions, hence causing a difference from the practical situation. With the removal of material, the residual stress is released and the deformation takes place towards equilibrium to give the larger deformation observed in the simulation. Moreover, the "unit life and death" method used in performing the simulation using ABAQUS does not take into account such elements as cutting force, cutting heat, among others.

Table 3: Path 1 radial deformation

Number	1	2	3	4	5	6	7	8
Measurement result	0	0	0.025	0.153	0.102	0.009	0.006	0.021
Simulation result	0.162	0.033	0.054	0.112	0.096	0.094	0.022	0.082

Table 4: Path 2 radial deformation

Axial distance	0	8.5	17.5	26.5	35.5	44.5	50.5
Measurement result	0.150	0.065	0.006	0.000	0.015	0.023	0.122
Simulation result	0.172	0.055	0.007	-0.002	0.018	0.085	0.171

In order to further verify the deformation direction of the member, Matlab was used to fit the coordinate data of 500 points measured by the CMM, and the experimentally measured deformation cloud map of the bottom surface of the member is shown in Fig. 2, which shows that the bottom surface of the member deforms inwardly with respect to the sidewalls, which is in the same direction of deformation as that of the simulation results.

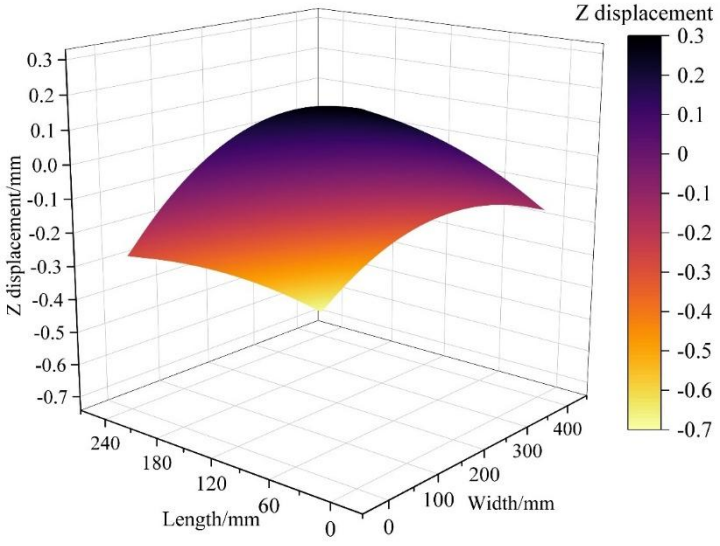

Figure 2: The component is deformed by the cloud

4 Quenching residual stress regulation methods

The maximum residual stress level in the aluminum alloy will mainly depend on the temperature history before the onset of plastic deformation. In this case, the most suitable

critical temperature for elastic-plastic transformation can be used as the node, while varying the cooling rate (heat transfer coefficient at the surface) in stages can solve the conflicting relationship.

4.1 Stress management methods

The pre-critical morphology of material governs the residual stress distribution in the end, whereas the convective heat transfer coefficient after the critical point affects only the speed at which the elastic deformation is recovered and does not influence the residual stress in any way. Hence, one can state that the temperature range between the solid-solution temperature and the critical temperature is the temperature range in which the residual stress is controlled, and that the internal temperature gradient can be effectively reduced through decreasing the convective heat transfer coefficient in the region, thus reducing residual stress levels; the region is called the stress control region. At the same time, since the temperature change at the stage of plastic deformation no longer influences the residual stress, the temperature range between the critical temperature and the room temperature can be considered as the temperature range controlling the material properties. The material properties will be preserved through proper adjustment of the convective heat transfer coefficient in this range, whereas the residual stress will stay constant; the temperature range is called the performance control region. For comparison of the effects of residual-stress control through various temperature ranges governed by the convective heat transfer coefficient, four typical convective heat transfer curves were developed with a critical temperature of 248° C. The convective heat transfer coefficients for the proposed schemes are summarized in Table 5.

Table 5: The convection heat transfer coefficient of different schemes

Temperature /°C	Scheme 1	Scheme 2	Scheme 3	Scheme 4
	Convection heat transfer coefficient($\times 10^6$kW($m^2\times$°C)$^{-1}$)			
50	2.4	18.2	2.4	23
100	4.2	17.4	4.2	21
150	9.5	17.4	9.5	20
200	13.4	17.4	13.4	18.5
250	17.4	17.4	17.4	17.5
275	16.6	16.6	2.7	6.2
300	16.2	16.2	2.7	4.5
350	13.1	13.1	3.2	3.8
400	11.4	11.4	3.3	3.4
450	9.2	9.2	3.4	3.1
500	7.1	7.1	3.5	3.0

As per the findings obtained from the quenching process simulation, the fluctuations observed in the cooling and equivalent plastic strain in the surface region as well as the core region of the specimens in each of the cases have been illustrated in Figures 3 and 4. Similarly, the figures 5(a) and 5(b) present the fluctuations in the residual stress distribution of all the four cases while the figures 5(a) and 5(b) represent those of the stresses along the rolling and transverse directions.

The profiles of the convective heat transfer coefficients have a significant impact on the variation in cooling rates. Since the surface layer is adjacent to the quenchant, its cooling rate shows more of a time-varying response than that of the core in terms of the convective heat transfer coefficient. Since the convective heat transfer coefficient is the same for the stress

control zone, the cooling rates of both the surface layer and the core for Scenarios I and II are similar, and their values are higher compared to Scenarios III and IV. At the same time, the plastic strain change values for Scheme I and Scheme II are almost similar, implying that the time taken to reach the critical temperature from the solid-solution temperature is almost the same for both schemes; hence, the cooling time in the stress control zone is the same. It can be stated that the residual stress evolution for Schemes I and II is almost identical; therefore, differences in the convective heat transfer coefficient in the performance control zone between the two schemes do not affect the residual stress evolution.

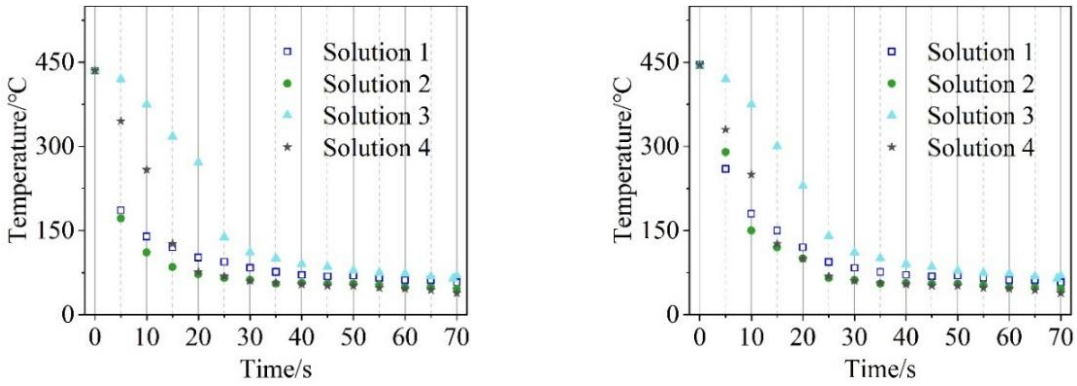

(a)Surface cooling (b)Core cooling

Figure 3: Cooling curve

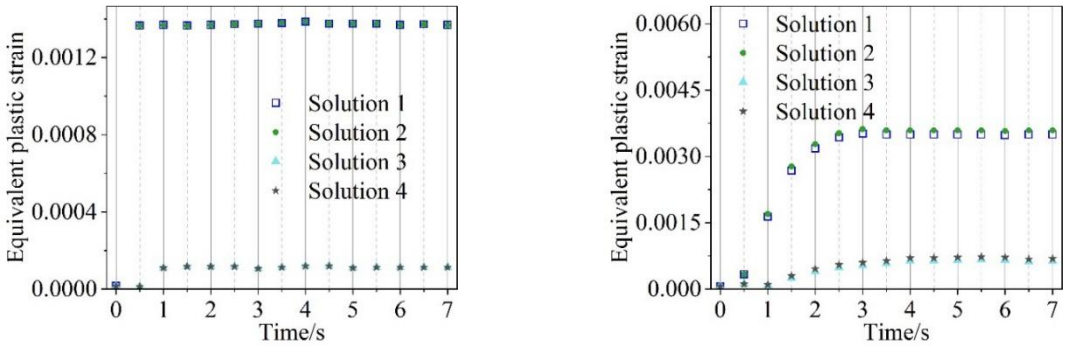

(a)Surface (b)Core

Figure 4: Lateral stress variation

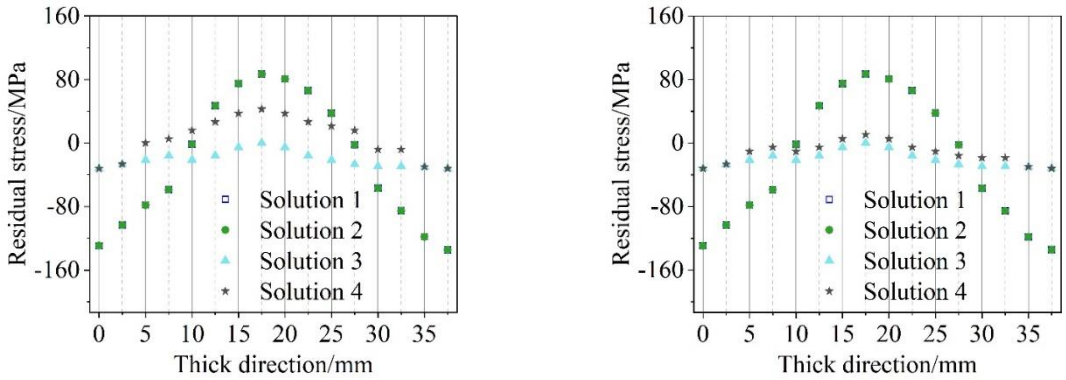

(a)Rolling direction stress (b)Lateral stress

Figure 5: The residual stress distribution of four kinds of schemes

4.2 Quenching Process Analysis

Residual stresses are relieved due to parameters related to the quenching procedure. These parameters are the type of quenching, temperature of quenching, the quenching medium, and its temperature. The main difference between the above quenching procedures is related to the differences between the convective heat transfer coefficients for various types of quenching processes. Convective heat transfer coefficient-temperature curves can be obtained using a spray quenching technique where the specimen's end-quenching surface is standard (50mm x 50mm; 170 mm long), in which the water temperature of the quenching medium is set to be 26 ℃, and the initial temperature of the specimen before quenching is set to be 475 ℃. The spacing between the temperature measurement points A and B was set to 6 mm, where the distance between point A and the quenched end face was also 6 mm. After the specimens were heated and kept warm, they were transferred from the heating furnace to the end quenching device and quenched. It has been proved that the specimen transfer time is too long will reduce the mechanical properties of the material, therefore, the whole specimen transfer time is not more than 5 s. Three different spray quenching process parameters were set, and the spray quenching process parameters are shown in Table 6. The corresponding convective heat transfer coefficient variations of these three schemes are shown in Fig. 6.

For the stress control region, Scheme I demonstrates a significantly higher heat transfer coefficient by convection relative to the other two schemes; therefore, the magnitude of the quenched residual stress for Scheme I is expected to be higher than that of the other two schemes. In addition, Scheme II shows a higher heat transfer coefficient by convection than Scheme III in the stress control region, thereby suggesting that Scheme II will have a higher quenched residual stress than Scheme III.

Table 6: Spray quenching process parameter

Quenching process	Solution 1	Solution 2	Solution 3
Nozzle flow Q /$Lm^{-2}s^{-1}$	105	120	65
Jet pressure p /kPa	200	100	20

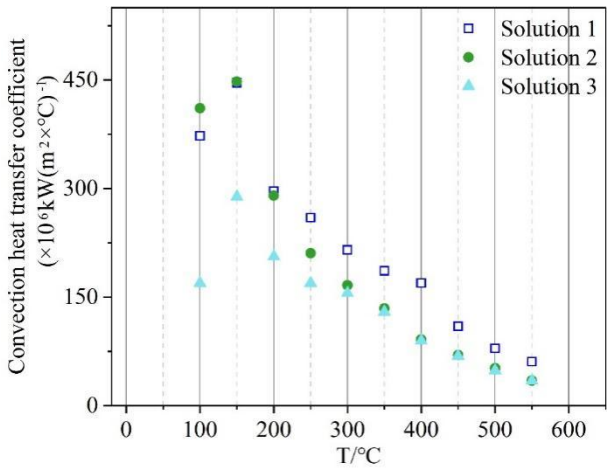

Figure 6: The convection heat transfer coefficient of quenching process schemes

Due to the different quenching process, it makes the three quenching schemes critical temperature differences, the critical temperature and cooling time as shown in Table 7. The critical temperature of Scheme I is 204℃, the critical temperature of Scheme II is 208℃, and the critical temperature of Scheme III is 249℃. However, overall, the differences in critical temperatures did not affect the prediction of quenching residual stresses.

Table 7: Critical temperature and cooling time

Quenching process	Critical temperature / ℃	Surface cooling time	Core cooling time
Solution 1	204	8.25	15.33
Solution 2	208	10.93	17.13
Solution 3	249	15.25	21.08

Comparative data on residual stress profiles for the three programs are summarized in Table 8 below. While the maximum stress levels in the rolling direction for programs 1 and 2 are fairly similar, variations still occur among the different quenching process programs in their residual stress profiles, but from the amplitude, whether rolling or transverse, program 1 is much larger than the remaining two programs. Scheme 2 and Scheme 3 two directions of residual stresses regardless of the amplitude or distribution trend are relatively close. Among them, the rolling direction stress amplitude of Scheme 2 is reduced by 9.48% compared with Scheme 1, and the stress amplitude in the transverse direction is reduced by 49.76%; the rolling direction stress amplitude of Scheme 3 is reduced by 9.89% compared with Scheme 2, and the stress amplitude in the transverse direction is reduced by 11.08%; it can be illustrated that the actual results of the quenching stresses have a very good consistency with the predicted results.

Table 8: Residual stress

Hardening process		Rolling direction	Lateral direction
Solution 1	Surface layer	-75.7	-92.41
	Core layer	181.18	107.33
	Stress amplitude	256.82	205.12
Solution 2	Surface layer	-60.67	-45.21
	Core layer	171.89	57.86
	Stress amplitude	232.48	103.06
Solution 3	Surface layer	-44.7	-41.49
	Core layer	164.83	51.08
	Stress amplitude	209.48	91.64

5 Conclusion

In this study, a finite-element framework was established to describe the evolution of residual stresses at the initial stage of quenching in high-strength aluminum alloys, and simulation analysis was performed to investigate an efficient strategy for regulating these stresses.

On the basis of the developed numerical framework and methodology, the prediction of quenching-induced stress in 7075 aluminum alloy showed high reliability, and the formation and evolution process was successfully captured. The discrepancy between simulation and experimental results remained within 6.52%-13.68%, and the predicted deformation pattern agreed well with the measured data, confirming the validity of the numerical approach and providing feasible guidance for subsequent process optimization.

The proposed regulation method, based on stress control zones and performance control zones, can effectively reduce the temperature gradient and stress magnitude by reasonably lowering the convective heat transfer coefficient in the stress control zone. Through this adjustment, the mechanical properties of the alloy in the performance control zone can be preserved without altering the distribution pattern of the final stress field, thereby enabling stress regulation through the above approach.

Quenching parameters exert a significant influence on stress distribution, among which the convective heat transfer coefficient is the most sensitive factor. It can be properly controlled

through nozzle flow, injection pressure, and other process-adjustment strategies to reduce stress amplitude. In program two and program one, the maximum reduction reached 49.76% compared with the transverse direction.

The proposed method enables efficient control of the initial stress state and provides both a theoretical foundation and practical guidance for process optimization in industrial production.

Funding

This research was supported by the Key Research Project Plan for Higher Education Institutions in Henan Province: “Research on Measurement and Control Methods for Initial Residual Stress in High-Strength Aluminum Alloys” (24A460019);

Natural Science Foundation of Henan Province: “Research on Coupling Dynamics Behavior and Fatigue Life of Fault Gear Transmission System” (242300420351).

References

[1] Zhang, Q., Zhu, Y., Gao, X., Wu, Y., & Hutchinson, C. (2020). Training high-strength aluminum alloys to withstand fatigue. Nature communications, 11(1), 5198.

[2] Mason, C. J. T., Rodriguez, R. I., Avery, D. Z., Phillips, B. J., Bernarding, B. P., Williams, M. B., ... & Allison, P. G. (2021). Process-structure-property relations for as-deposited solid-state additively manufactured high-strength aluminum alloy. Additive manufacturing, 40, 101879.

[3] Dixit, S., & Liu, S. (2022). Laser additive manufacturing of high-strength aluminum alloys: challenges and strategies. Journal of Manufacturing and Materials Processing, 6(6), 156.

[4] Jiang, L., Wang, C., Fu, H., Shen, J., Zhang, Z., & Xie, J. (2022). Discovery of aluminum alloys with ultra-strength and high-toughness via a property-oriented design strategy. Journal of Materials Science & Technology, 98, 33-43.

[5] Guo, X., Li, H., Xue, P., Pan, Z., Xu, R., Ni, D., & Ma, Z. (2023). Microstructure and mechanical properties of 600 MPa grade ultra-high strength aluminum alloy fabricated by wire-arc additive manufacturing. Journal of Materials Science & Technology, 149, 56-66.

[6] Chemin, A. E. A., Afonso, C. M., Pascoal, F. A., Maciel, C. D. S., Ruchert, C. O. F. T., & Bose Filho, W. W. (2019). Characterization of phases, tensile properties, and fracture toughness in aircraft-grade aluminum alloys. Mater. Des. Process. Commun, 1(4), 1-13.

[7] Dwivedi, P., Siddiquee, A. N., & Maheshwari, S. (2021). Issues and requirements for aluminum alloys used in aircraft components: state of the art. Russian Journal of Non-Ferrous Metals, 62(2), 212-225.

[8] Zhou, B., Liu, B., & Zhang, S. (2021). The advancement of 7xxx series aluminum alloys for aircraft structures: A review. Metals, 11(5), 718.

[9] Xiong, B., Yan, H., Zhang, Y. A., Li, Z., & Li, X. (2023). Development strategy for the

aviation-grade aluminum alloy industry in China. Strategic Study of Chinese Academy of Engineering, 25(1), 88-95.

[10] Lu, Y., Zhu, S., Zhao, Z., Chen, T., & Zeng, J. (2020). Numerical simulation of residual stresses in aluminum alloy welded joints. Journal of Manufacturing Processes, 50, 380-393.

[11] Zheng, Y., Tian, Y., Ma, J., Zhang, F., Cui, X., & Ren, L. (2024). Residual stress formation mechanism considering cutting energy in milling of 7075 aluminum alloy. The International Journal of Advanced Manufacturing Technology, 131(5), 3039-3055.

[12] Xue, N. P., Wu, Q., Yang, R. S., Gao, H. J., Zhang, Z., Zhang, Y. D., ... & Guo, J. (2023). Research on machining deformation of aluminum alloy rolled ring induced by residual stress. The International Journal of Advanced Manufacturing Technology, 125(11), 5669-5680.

[13] Yi, S., Wu, Y., Gong, H., Peng, C., & He, Y. (2021). Experimental analysis and prediction model of milling-induced residual stress of aeronautical aluminum alloys. Applied Sciences, 11(13), 5881.

[14] Zhang, Z., Huang, W., Lu, G., & Zhang, Y. (2020). Spatial distribution evolution of residual stress and microstructure in laser-peen-formed plates. Materials, 13(16), 3612.

[15] Teng, L., Lu, X., Zhang, H., & Zhang, G. (2025). Simulation and Experiment Analysis of Residual Stress Distribution Law in FSW Joint of 2219-T8 Aluminum Alloy Thick Plate. Experimental Techniques, 1-17.

[16] Wu, Q., Wu, J., Zhang, Y. D., Gao, H. J., & Hui, D. (2019). Analysis and homogenization of residual stress in aerospace ring rolling process of 2219 aluminum alloy using thermal stress relief method. International Journal of Mechanical Sciences, 157, 111-118.

[17] Ma, Y., Xue, N., Wu, Q., Gao, H., & Wu, J. (2020). Residual stress analysis of a 2219 aluminum alloy ring using the indentation strain-gauge method. Metals, 10(7), 979.

[18] Zheng, J., Shang, Y., Guo, Y., Deng, H., & Jia, L. (2022). Analytical model of residual stress in ultrasonic rolling of 7075 aluminum alloy. Journal of Manufacturing Processes, 80, 132-140.

[19] Xu, Y., Yue, C., Chen, Z., Li, M., Wang, L., & Liu, X. (2023). Finite element simulation of residual stress in milling of aluminum alloy with different passes. The International Journal of Advanced Manufacturing Technology, 127(9), 4199-4210.

[20] Li, X., Tang, X., Li, M., Liu, Q., Tuo, Z., Cao, Q., & Li, L. (2025). Relaxation of residual stress in aluminum alloy rings by pulsed high magnetic field: Relieving mechanisms and performance evaluation. Journal of Materials Processing Technology, 338, 118778.

[21] Xu, Y., Shi, Z., Li, B., & Zhang, Z. (2021). Effects of TVSR process on the dimensional stability and residual stress of 7075 aluminum alloy parts. Reviews on Advanced Materials Science, 60(1), 631-642.

[22] Ye, S., Chen, K., Zhu, C., & Chen, S. (2019). A New Path of Quench-Induced Residual

Stress Control in Thick 7050 Aluminum Alloy Plates. Metals, 9(4), 393.

[23] Zhang, M., Gu, K., Weng, Z., Cui, C., & Wang, J. (2024). Residual stress evolution of 7050 aluminum alloy during thermal processing and its effects on processing deformation and mechanical properties. Journal of Materials Engineering and Performance, 33(21), 11467-11483.

[24] Chen, H., Tang, P., Xie, Y., Ren, Y., Wang, M., & Mo, L. (2025). Optimization of Residual Stress Microstructure and Mechanical Properties in 7075 Aluminum Alloy Via Annealing. Journal of Materials Engineering and Performance, 1-14.

[25] Li, Y., Zhao, G., Liu, L., Cao, S., & Sun, Y. (2025). Investigation on the effect of stress relaxation aging on the reduction of quenching residual stress in 7055 aluminum alloy profiles. Materials Characterization, 115439.

[26] Pan, X., Zhou, L., Wang, C., Yu, K., Zhu, Y., Yi, M., ... & Liang, X. (2023). Microstructure and residual stress modulation of 7075 aluminum alloy for improving fatigue performance by laser shock peening. International Journal of Machine Tools and Manufacture, 184, 103979.

[27] Qi, S., Huang, G., Xu, X., Zhang, H., Dai, D., Xi, L., ... & Gu, D. (2024). Effect of laser process parameters on thermal behavior and residual stress of high-strength aluminum alloy processed by laser powder bed fusion. Journal of Materials Research and Technology, 33, 3756-3768.